Damage localisation using transient nonlinear elastic wave spectroscopy on composite structures

G. Zumpano, M. Meo

G. Zumpano, M. Meo. Damage localisation using transient nonlinear elastic wave spectroscopy on composite structures. International Journal of Non-Linear Mechanics, Elsevier, 2008, 43 (3), pp.217. 10.1016/j.ijnonlinmec.2007.12.012 . hal-00501771

Author's Accepted Manuscript

Damage localisation using transient nonlinear elastic wave spectroscopy on composite structures

G. Zumpano, M. Meo

www.elsevier.com/locate/nlm
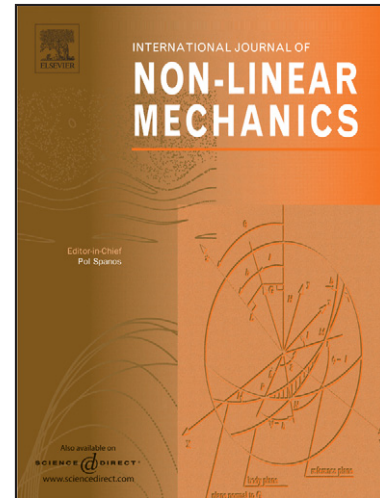
Cite this article as: G. Zumpano and M. Meo, Damage localisation using transient nonlinear elastic wave spectroscopy on composite structures, *International Journal of Non-Linear Mechanics* (2007), doi:10.1016/j.ijnonlinmec.2007.12.012

DAMAGE LOCALISATION USING TRANSIENT NONLINEAR ELASTIC WAVE SPECTROSCOPY ON COMPOSITE STRUCTURES

G. Zumpano [*], M. Meo [+1]
[*] Department of Engineering, Cambridge University,
Trumpington Street, Cambridge CB2 1PZ

[+] Department of Mechanical Engineering,
University of Bath, Bath BA2 7AY, UK

Abstract

To reduce the costs related to maintenance of aircraft structures, there is the need to develop new robust, accurate and reliable damage detection methods. A possible answer to this problem is offered by newly developed nonlinear acoustic/ultrasonic techniques, which monitors the nonlinear elastic wave propagation behaviour introduced by damage, to detect its presence and location.

In this paper, a new Transient Nonlinear Elastic Wave Spectroscopy (TNEWS) is presented for the detection and localization of a scattered zone (damage) in a composite plate. The TNEWS analyse the uncorrelations between two structural dynamic responses generated by two different pulse excitation amplitudes by using a time-frequency coherence function. A numerical validation of the proposed method is presented. Damage was introduced and modelled using a multi-scale material constitutive model (Preisach-Mayergoyz space).

The developed technique identified in a clear manner the faulted zone, showing its robustness to locate and characterize nonlinear sources in composite materials.

1. Introduction

Composite materials are well renowned for their high strength weight ratio that makes them the ideal solution for aircraft structures, where weight is a primary issue. However, composite material fragility to foreign object impacts, often leads to barely visible damages which may reduce the structure strength of a staggering 50% [1], is becoming a crucial factor for the aeronautic industries. The impact damage causes a structural strength reduction which can drive the structure to collapse if the damage presence and location are not promptly identified.

In the last few decades, a number of acoustic/ultrasonic damage detection techniques were developed to analyse the changes of linear properties due to the presence of damage. In particular, linear acoustic/ultrasonic methods study the changes of wave speed, waves reflection and refraction, and/or signal amplitude changes to assess the presence and location of structural anomalies.

Currently, a new class of promising NDE techniques, called non-linear elastic wave spectroscopy (NEWS) is being developed and it monitors the integrity of structures by analysing the material nonlinear elastic behaviour [2-10] caused by the presence of damage. These methods [2-10] appear to be more effective than linear acoustic methods since they are able to detect microcracks long before changes of linear acoustic properties.

So far, the exploitation of material nonlinear elastic properties has involved only the detection of damage presence (without any attempt to locate the damage) using either a mono or a bi harmonic stationary excitation. Numerical and experimental examples of such

---

[1] m.meo@bath.ac.uk

approach are given by the SINMORAS (low frequency mono-harmonic excitation [11]), and the Nonlinear Wave Modulation Spectroscopy (NWMS, bi-harmonic excitation used to study sand stones [2], stress corrosion cracking in welded plates [12] and sandwich plates [10]). A first numerical attempt aimed at the analysis of material nonlinear elastic properties using transient structure excitations was carried out by the authors [13], who investigated the effects of four different damage shapes on a Gaussian shaped pulse propagating on an aluminium plate. This work made clear that waves propagating through the structure retain non-classical nonlinear elastic behaviour if reflected or refracted by damage. This result was exploited by the authors in the development of the nonlinear elastic wave self focusing approach employing time reversal mirrors [14]. However, issues related to shadowing effects of the most severe damages leading to misdetection of smaller damages have brought the research to focus on tomographic like approaches which are capable of generating an image of the structure under investigation and potentially able to detect without any limit, multi-site damages.

A new Transient Nonlinear Elastic Wave Spectroscopy (TNEWS) is being presented in this paper. The methodology analyse the changes in transient structural dynamic responses [13] due to the nonlinear material behaviour due to the damage presence. In particular, the method analyse the discrepancies in the times signal between two structural dynamic responses generated by two different pulse excitation amplitudes by using a time-frequency coherence function [22].

The proposed method was evaluated numerically on a composite panel. The paper presents firstly an overview of the material nonlinear elastic behaviour and, then, the proposed damage detection methodology.

2. Material nonlinear elastic wave behaviour

Experimental evidences [2-10] showed that classical nonlinear models [15] cannot explain the nonlinear behaviour generated by local nonlinear forces due to damage presence (such as cracks, voids, and contacts). A theoretical description of this behaviour can be given by the nonlinear mesoscopic elastic material model, which contains terms that describe classical nonlinearity, as well as hysteresis, and discrete memory [2-4]. This is possible by adding to the nonlinear classical stress strain relationship, a stress dependence on strain time derivative [2-10]:

$$\sigma = \int E\left(\varepsilon, \dot{\varepsilon}\right) d\varepsilon \qquad (1)$$

where E is the nonlinear and hysteretic modulus given by:

$$E\left(\varepsilon, \dot{\varepsilon}\right) = E_0 \left\{ 1 - \beta\varepsilon - \delta\varepsilon^2 - \alpha\left[\Delta\varepsilon + \varepsilon\left(t\right)\text{sign}\left(\dot{\varepsilon}\right) + \dots \right] \right\} \qquad (2)$$

where E_0 is the linear modulus, $\Delta\varepsilon$ is the strain amplitude change over the last period, β and δ classical nonlinear coefficients, and α a material hysteresis measure. The full spectrum of options given by the equation (2) is summarized in [2]. Experimental and numerical evidences [2-10] showed that the 3rd harmonic has quadratic behaviour with the fundamental amplitude for a purely hysteretic material and cubic according to classical nonlinear theory. Moreover, a second-order sideband $f_2 \pm 2 f_1$, generated by a bi-tone excitation (f_1 and f_2) has amplitude proportional to $\alpha A_1 A_2$ for a purely hysteretic material, in contrast with an amplitude dependence proportional to $C(\beta, \delta)A_1^2 A_2$ for a classical nonlinear material. For a

classical nonlinear material, the first order sideband ($f_2 \pm f_1$) amplitude is linear with the excitation amplitudes $\beta A_1 A_2$., and it is absent for purely hysteretical material [12].

Due to the inadequacy of classical non linear material model to reproduce the behaviour of microcracked damaged materials, a new material constitutive model, based on Presaich and Mayergoyz (PM) space, capable of accurately describing the nonlinear, discrete memory and hysteretic behavior of such materials, was implemented in a Fortran FE code written by the authors.

3. Presaich and Mayergoyz space

Non classical nonlinear elastic material behavior (hysteresis and material memory) can be described by a nonlinear mesoscopic elastic material model such as the Preisach-Mayergoyz (P-M) [16-17]. According to this approach, the macroscopic behavior (Figure 1) of damaged materials is described by the contribution of a number of mesoscopic material cells (1-10 mm), which are composed by a statistical collection of microscopic units (1-100 μm) with varying properties defining their stress-strain relation. The strain of these microscopic units is a combination of a classical non-linear state relation (elastic component contribution), and a non-classical addition due to hysteretic effects (interface binding contribution). In particular, the strain component of Hysteretic Mesoscopic Elastic Unity (HMEU) can be thought as the strain of a micro-crack when subject to an external pressure that produces its closing and opening (Figure 2). This two stage behavior is highlighted in Figure 3-a, in case of non classical nonlinear elastic behavior contribution. The pressure-displacement of microcracks is characterised by a rectangular loop defined by two couples of parameters: the two equilibrium lengths (l_o, l_c) and a pair of pressure (P_c, P_o) with $P_c \geq P_o$.
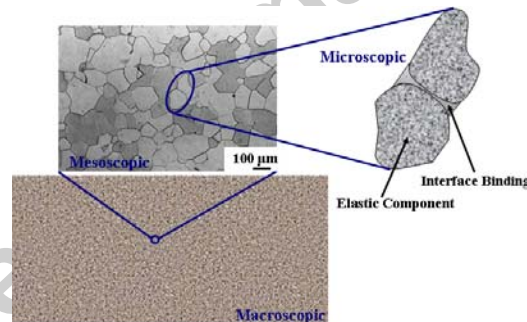

Figure 1 - Mesoscopic model (Microstructure of the single-phase LCB titanium alloy [18])
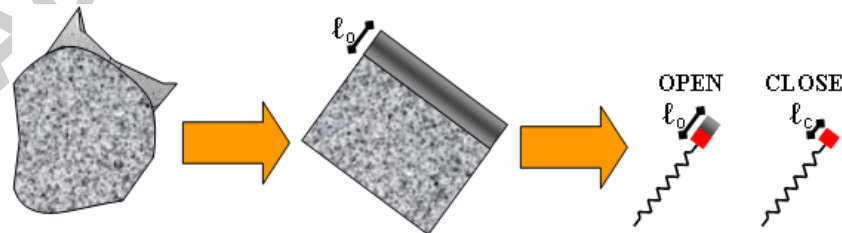
Figure 2 – Hysteretic Mesoscopic Elastic Unity.

According to the rectangular loop (Figure 3-a), the equilibrium length of the interface binding remains constant (ℓ_o) until the pressure load equals the closing pressure P_c (ℓ_c), therefore, the only length changes of the HMEU are those of its elastic component. For pressure loads above the closing pressure P_c, once again, the only length changes are those of the HMEU elastic component. Then, decreasing the pressure load P, the HMEU length changes are only due to the HMEU elastic component until the pressure P reaches the opening

pressure P_o, where the HMEU interface binding elongates to ℓ_o, and remains constant until the pressure is reversed and increases to P_c.

The HMEU distribution of a material is represented in a stress–stress space (P_c, P_o), commonly termed "PM-space". This representation is defined mathematically by specifying its density distribution $\mu(P_c, P_o)$ (see Figure 3-b for a Gaussian distribution). The PM space representation of real materials can be derived using quasistatic measurements of the material strain according to specifically designed protocol loads [16-17].
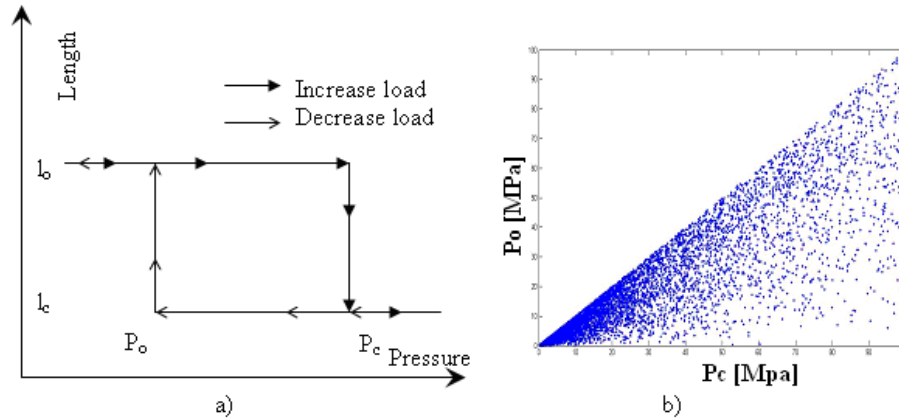

Figure 3: a) Behaviour of HMEU; b) Example of PM-space.

From the HMEU properties above described and their PM space distribution, it is clear that the actual number of HMEUs closing or opening, at every instant, depends on the previous load history of the material and on the sign of the applied pressure ΔP.

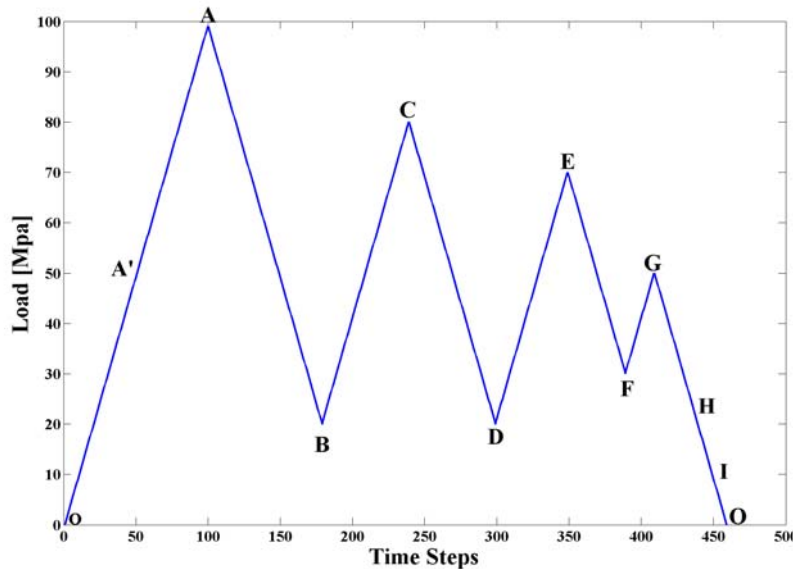**Figure 4 – Load Protocol.**

For example, if the load history represented in Figure 4 is applied to the material described in Figure 3-b, the resulting stress-strain curve (Figure 5) is evaluated as described below.

The HMEU closed for $P_o=0$ (point O, Figure 4) is zero. Therefore, the associated strain is zero. Increasing the pressure load to point A' (Figure 4) all the HMEUs contained in the black

triangle (Figure 6-a) close. Therefore, the strain due to the pressure load P_A' can be evaluated as the difference between the averaged length of all HMEUs at P_A' ($\ell(P_A')$) and the HMEU length ℓ_o, divided ℓ_o.

$$\varepsilon\left(P_{A'}\right)=\frac{l\left(P_{A'}\right)-l_o}{l_o} \qquad (3)$$

with

$$l\left(P_{A'}\right)=\frac{l_o\left(1-N_c\right)+l_cN_c}{N}=\frac{l_o\left(1-\kappa N_c\right)}{N}=l_o\left(1-\kappa F_c\right) \qquad (4)$$

where:
- N_c is the number of HMEUs closed.
- N is the total number of HMEUs.
- F_c is the fraction of closed HMEUs
- κ is the maximum strain obtainable if all HMEUs close.

Therefore, by substituting the last member of eq. (4) into eq. (3), the strain can be evaluated as:

$$\varepsilon\left(P_{A'}\right)=-\kappa F_c \qquad (5)$$

Bringing the pressure load to P_A all the HME units enclosed in the orange trapezium (Figure 6-a) close as well, so an increase of strain is obtained (Point A in Figure 5).

Reducing the pressure load to P_B, all the HME units having an opening pressure P_o higher than P_B open (see dashed triangle in Figure 6-b). Therefore, the number of HME units closed reduce and, so, the strain (Point B in Figure 5). A subsequent increase of pressure load to P_C determines the closing of the HME units enclosed in the yellow triangle of Figure 6-c and, therefore, an increase of strain to point C, in Figure 5. The following decrease of pressure load to $P_D=P_B$ determines the opening of HME units closed at the previous stage (see dashed triangle in Figure 6-d), so as, the strain level recorded at P_B is reinstated and the material memory property reproduced (Point D in Figure 5).

The increasing of pressure load to P_E brings to the closure of all HME units having P_c smaller than P_E (yellow triangle in Figure 6-e) and, consequently, an increase of strain is obtained (Point E in Figure 5). The following pressure load reduction to P_F, then, its increase to P_G and, finally, its decrease to P_H (Figure 6-f – Figure 6-h) cause a strain change that describes an inner hysteretic loop (F-G loop in Figure 5) of the hysteretic loops B-C and B-E.
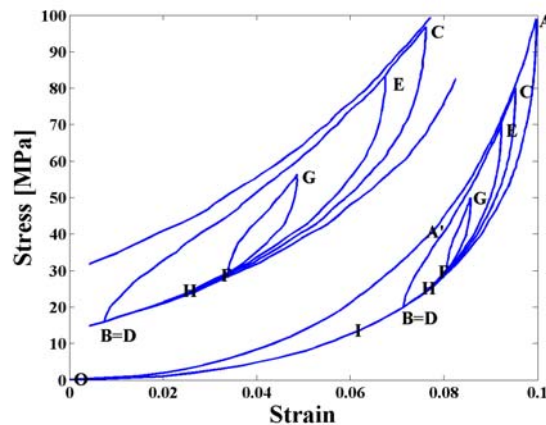

Figure 5 – Stress-strain curve.

The further reduction of the pressure load to P_I first and, then, to P_O determine, respectively, the closure of the hysteretic loop B-E and O-A (Figure 6-h). From the example above illustrated, it is clear that according to the PM space model, the material memory is limited to those pressure loads identified by the $MAT_{Hystory}$ line (blue step line in Figure 6-g). Therefore, in the material FE model implemented in the house FE code, only those pressure loads, defined by the $MAT_{Hystory}$ line, were stored in memory.

At the aim to save computational time, the PM space based material model was designed to evaluate directly the hysteretic contribution to the material elastic modulus.

This task was accomplished by evaluating at each time step, the increase of pressure load ΔP and, then, knowing the $MAT_{Hystory}$ line, the number of HME units that open ($\Delta P<0$) or close ($\Delta P>0$) is evaluated and, so, the strain change $\Delta\varepsilon$ (eq. 5). Hence, the hysteretic contribution to the material elastic modulus is evaluated as follows:

$$E_H = \frac{\Delta P}{\Delta\varepsilon} \qquad (6)$$

The material nonlinear macroscopic behaviour can be imagined to be made by a large
number of units characterised by different couples of (P_c, P_o). The distribution of HMEU in the plane (P_c, P_o) of the macroscopic entity is localised below a 45 degree line, since P_c must be larger than P_o as displayed in Figure 3-b. The HMEU are usually represented in a stress–stress space, commonly termed ''PM-space'', according to their values P_c and P_o. This representation is defined mathematically by specifying its density distribution $\mu(P_c, P_o)$.
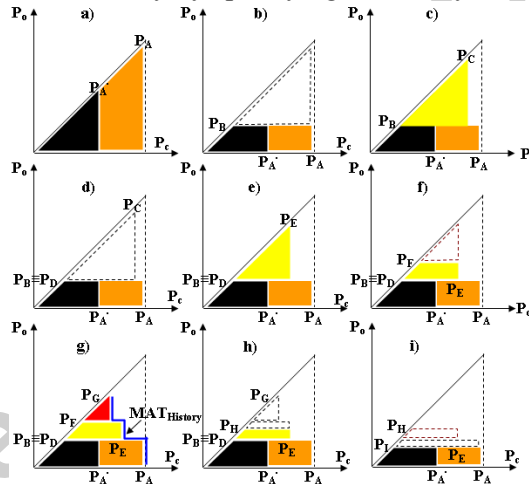

Figure 6 – Close HMEU history log.

The distribution of the HMEU on the (Pc,Po) plane can be derived using quasistatic measurements of the material strain according to specifically designed protocol loads [8-9]. Applying a certain load protocol, a change of the applied pressure ΔP occurs and, therefore, a certain number of HMEU closes or opens consistently with their characteristic pressures (P_c, P_o). Once the number of the HMEU units closed is known, the non-classical correction K_1 of the classical nonlinear elastic modulus E can be evaluated as follows:

$$\frac{1}{K_1} = -\frac{1}{L(P)}\frac{L(P+\Delta P)-L(P)}{\Delta P}; \quad P \circledR P+\Delta P$$

$$\frac{1}{K_1} = -\frac{1}{L(P)}\frac{L(P)-L(P-\Delta P)}{-\Delta P}; \quad P \circledR P-\Delta P \qquad \mathbf{(7)}$$

where the term L(P) (eq. 1) is the length of the specimen, and P is the applied pressure.

$$L(P)=N_c(P)\times l_c+\left(N-N_c(P)\right)\times l_o$$
$$L(P+\Delta P)=N_c(P+\Delta P)\times l_c+\left(N-N_c(P+\Delta P)\right)\times l_o \qquad (8)$$
$$L(P-\Delta P)=N_c(P-\Delta P)\times l_c+\left(N-N_c(P-\Delta P)\right)\times l_o$$

where N is the total number of HMEU, $N_c(P)$ is the number of HMEU closed when the pressure is P, and ℓ_c and ℓ_o are the equilibrium lengths of HMEU. Therefore, considering only the contribution of the HMEU to the material deformation, the strain generated by a stress P is given by the following expression:

$$\varepsilon=\frac{L(P)-L_0}{L_0} \qquad (9)$$

where L_0 is the initial length of specimen.

4. Nonlinear FE code

The above described nonlinear elastic material constitutive law was implemented in our in-house FE code to simulate the presence of damage in structures. The equation of motion for a FE discretised structure are:

$$[M]\{\ddot{d}\}_n+[D]\{\dot{d}\}_n+[K]_n\{d\}_n=\{R^{ext}\}_n$$
$$[M]=\sum_e\int_{V_e}\rho[N]^T[N]dV \quad [D]=\sum_e\int_{V_e}\kappa_d[N]^T[N]dV \qquad (10)$$
$$[K]_n=\sum_e\int_{V_e}\rho[B]^T[E]_n[B]dV$$

where:
- [M] and [D] are, respectively, the mass and damping matrix of the structure.
- $[K]_n$ is the stiffness matrix at the nth time step.
- $[E]_n$ is the stress strain matrix for the finite element e at the nth time step.
- $\{d\}_n$ is the displacement vector at the nth time step.
- $\{R^{ext}\}_n$ is the external force vector at the nth time step.
- [N] is the matrix of shape functions.
- [B] is the strain displacement matrix.
- κ_d is the material damping parameter for the finite element e.
- ρ is material density
- V_e is the element volume.
- $\sum_e$ stands for the assembling of all elements in which the structure was discretised.

The stiffness matrix was calculated as the sum of a linear elastic term $[K_{lin}]$ and a nonlinear perturbation force $\{R^{int}\}_n$:

$$[K]_n\{d\}_n=[K_{lin}]\{d\}_n+\{R^{int}\} \qquad (11)$$

where the nonlinear perturbation force was evaluated as:

$$\left\{R_e^{int}\right\} = \int_{Ve} [B]^T \left\{\Delta\sigma\right\}_n dV$$
$$\left\{\Delta\sigma\right\}_n = \left([E]_n - [E]_{lin}\right)\left\{\varepsilon_e\right\}_n$$

(12)

where $[E]_{lin}$ is the material linear elastic stress-strain matrix and $\{\varepsilon_e\}_n$ element strain vector evaluated at the time step n. The evaluation of the stress strain matrix at the nth time step ($[E]_n$) is illustrated below for a 2D plane strain case in the case of anisotropic material. The first step consists in the evaluation of the strain vector:

$$\left\{\varepsilon\right\}_n = [B]\left\{d\right\}_n - \left\{\varepsilon^{in}\right\}$$

(13)

with $\{\varepsilon^{in}\}_n$ pre-strain and or thermal strain contribution. In the second step, the stress contribution for each coefficient of the stress strain matrix is evaluated:

$$\sigma_{11} = Q_{11}\varepsilon_{11}$$
$$\sigma_{12} = Q_{12}\varepsilon_{22}$$
$$\sigma_{22} = Q_{22}\varepsilon_{22}$$
$$\sigma_{66} = Q_{66}\varepsilon_{12}$$

(14)

$$[E]_{n-1} = \begin{bmatrix} Q_{11} & Q_{12} & 0 \\ Q_{12} & Q_{22} & 0 \\ 0 & 0 & Q_{66} \end{bmatrix} \quad ; \quad \left\{\varepsilon_e\right\}_n = \begin{Bmatrix} \varepsilon_{11} \\ \varepsilon_{22} \\ \varepsilon_{12} \end{Bmatrix}$$

where $[E]_{n-1}$ is the stress strain matrix for the finite element e at the $(n-1)^{th}$ time step. Then, the four independent material coefficients of $[E]_n$ are evaluated by inputting element stress contributions σ_{ij} in their respective PM spaces together with their previous load histories. As results of such procedure, the FE equation of motion assumes the following shape:

$$[M]\left\{\ddot{d}\right\}_n + [D]\left\{\dot{d}\right\}_n + [K]\left\{d\right\}_n = \left\{R^{ext}\right\}_n - \left\{R^{int}\right\}_n$$

(15)

The time integration of eq. (15) was provided by the Newmark method using a conjugate gradient solver [19-21].

5. Continuous wavelet transform

One of main drawbacks of the standard ultrasonic techniques, developed in either the time or the frequency domain [22-23], is that their performances decrease consistently in presence of echo overlaps, attenuation phenomena at high frequencies and critical sampling. These limitations can be overcome using Time Frequency Representations (TFRs) [23], which decrease the attenuation phenomena, and allows a careful control between overlapped echoes resulting in an increased accuracy of the measures.

The two most common TFRs, the Short Time Fourier Transformation (STFT) and the Continuous Wavelet Transformation (CWT) were investigated. Between those two, the CWT was chosen because of its better time resolution at high frequency and noise withstanding.

Wavelets are the natural evolution of STFTs [24-25]. They linearly decompose an arbitrary signal s(t) by projecting it on functions that are simply dilations and translations of a parent (or mother) wavelet g(t) via the convolution of the signal and the scaled/shifted parent wavelet [25-26]:

$$CWT(a,t) = \frac{1}{\sqrt{a}} \int_{-\infty}^{\infty} s(\tau) g^* \left(\frac{t-\tau}{a} \right) d\tau \qquad (16)$$

where a is the dilation parameter and τ is the translation parameter. Selecting a mother wavelet for a particular task is not easy, because of the countless parent wavelets (or mother wavelet) present in literature, applied to the most various problems. However, complex Morlet wavelets [26-30] are the most used, because they are capable of providing very useful information to visualize possible discontinuities such as magnitude and phase components of the signal time-frequency discretization. Moreover, this wavelet family becomes very attractive for harmonic analysis due to its analogy with the Fourier transforms expressed by this equation [26]:

$$g(t) = \frac{1}{\sqrt{\pi \gamma}} e^{-\frac{t^2}{\gamma}} \left(\cos(\omega_0 t) + i \sin(\omega_0 t) \right) \qquad (17)$$

Basically, Morlet wavelets are Gaussian-windowed Fourier transforms, with a central frequency $f_0 = \omega_0/2\pi$ and a width of the Gauss curve (wavelet frequency band) γ. By maximising eq. (14) in the frequency domain (eq. (16) [26] a unique relation between the dilation parameter a and frequency f is obtained:

$$f = \frac{a}{f_0} \qquad (18)$$

$$G(af) = e^{-\pi^2 \gamma (af - f_0)} \qquad (19)$$

Hence, because of this unique relation the Morlet wavelet was chosen as parent wavelet.

6. Damage detection methodology

A Transient Nonlinear Elastic Wave Spectroscopy (TNEWS) was designed, which should become in a near future the core of Nonlinear Elastic Wave Tomography. The TNEWS exploits changes in transient structural dynamic responses [13] due to the nonlinear behaviour introduced into the structure by the damage presence. The uncorrelations (discrepancies) between two structural dynamic responses generated by two different pulse excitation amplitudes are highlighted by a time-frequency coherence function [22]. As result, the arrival (at the sensor locations) of nonlinear elastic waves (generated by the Gaussian pulse wave impinging in the damage) will be observed in the time-frequency space with behaviours resembling those typical of structural change scattering mechanisms (Figure 7), though, the largest uncorrelations will be found around the harmonics of the excitation Gaussian pulse central frequency.
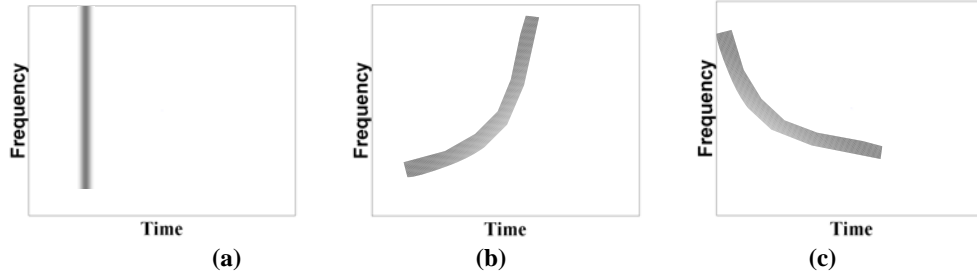
Figure 7 – Structural change scattering mechanisms: (a) surface discontinuity; (b) Material dispersion; (c) Waveguide structures.

Therefore, the damage presence can be detected by the uncorrelation formations in the time-frequency space, while the damage location is predicted by the use of a ray-tracing algorithm [22].

7. Transient Nonlinear Elastic Wave Spectroscopy

Transient Nonlinear Elastic Wave Spectroscopy (TNEWS) was developed out of the Wave Propagation Based Damage Detection (WPBDD) algorithm devised by the authors [22]. The WPBDD methodology is articulated in three steps. In the first step, the presence of the damage on the structure is assessed. In the second step, the arrival time of the reflected wave (or echo) can be estimated, and in the third step the damage location through a simplified Ray-Tracing algorithm is detected. The TNEWS was structured in a similar way and exploited similar algorithms. The fundamental difference lies in the selection of the two signals used for the damage detection process. In the WPBDD approach, a time signal acquired on the undamaged structure was used as reference signal for second time signal acquired by the structure monitoring system. With the TNEWS, there is no need to scan the undamaged structure, since the time signal generated by a low amplitude Gaussian pulse excitation (A_1) is used as the reference signal for a second time signal generated by a larger pulse amplitude (A_2).

7.1. The TNEWS process

The damage detection procedure consists in three steps: the acquisition, the damage presence detection and the damage localisation step. As an example, consider a section of a plate clamped along its short edges (Figure 8).
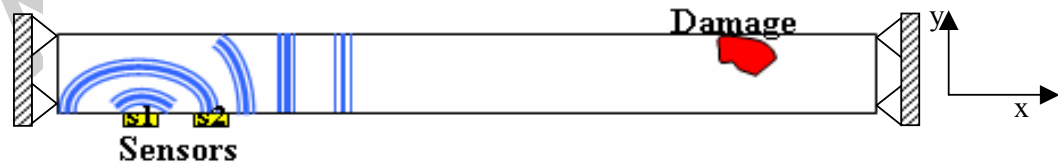

Figure 8 – Plate section.

In the acquisition step, two sensors (s1 and s2) are employed. The first sensors is used also to generate a perturbation wave (Gaussian pulse), which propagates through the plate to the damage location. A portion of the perturbation wave energy is reflected back towards the sensor locations, where is acquired by both sensors.

To increase the Signal Noise Ratio (SNR), the structure responses acquired by the two sensors were averaged over several measurements for both the reference and the large amplitude excitation Gaussian pulses, respectively, A_1 and A_2, with $A_2 > A_1$.

In the second step (damage presence detection step), the Coherence Function Based Algorithm (CFBA, see §7.2) analyses both Gaussian pulse acquired signals to seek for particular time-frequencies features revealing the arrivals of the damage reflected waves and, therefore, the damage presence. This operation is performed for acquired time signals of each sensor for the two different amplitudes of the Gaussian pulse used. Then, the arrival times of the first reflected wave by the structure defects is extracted for both the sensors ($t_{s1}(f)$ and $t_{s2}(f)$). Considering the sensor relative distance d_{12} and the perturbation wave travelling path parallel to x direction (Figure 8), the damage location (with respect to sensor 1) is estimated by the following expression:

$$d(f) = \frac{d_{12}}{t_{s1}(f) - t_{s2}(f)}(t_{s1}(f) - T) \qquad (20)$$

where f is the frequency, T is half time length of the excitation pulse. The half time length of the Gaussian pulse was subtracted to the arrival time of the damage reflected wave in sensor 1, because the acquisition time is set to start when the excitation begins, while the arrival times are estimated along the maxima lines corresponding to the maximum of the Gaussian pulse.

7.2. Coherence Function Based Algorithm

Structural damage (e.g. cracks, plasticization and corrosion) introduces nonlinear discrepancies in the dynamic response of structures perturbed by excitation pulses, which appear in the TFR as either vertical lines or slanted lines [24] (Figure 7). However, perturbation waves reflected back by the structure boundaries are expected to show a similar behaviour. This makes the work of conventional UT inspectors very complicated, requiring a great deal of experience for the discrimination of structural change features from those due to boundaries. Therefore, at the aim to simplify the interpretation of the ultrasonic signals a function (the coherence function) capable of highlighting the time discrepancy between the damaged and undamaged signal was employed [22]. Both linear and nonlinear changes associated to the damage presence can be picked up by the coherence function. However, nonlinear component due to defect presence can be highlighted by increasing the excitation amplitude [2-10, 11-14]. This peculiarity makes possible the use of two time signals generated by the same Gaussian pulse but with two different amplitudes (A_1, A_2) with $A_2 > A_1$. The Coherence Function Based Algorithm (CFBA), previously developed by the authors [22], was used.

This is articulated in two steps. The first step involves the evaluation of a time-frequency coherence function, while the second phase identifies the presence of damages by discriminating between the time-frequency coherence changes due to noise and damage reflected wave arrivals.

In the first phase of the CFBA, the time frequency coherence function, between the structure dynamic responses $s_1(t)$ and $s_2(t)$ generated by excitation pulses of magnitudes A_1 and A_2, is evaluated as the ratio of the wavelet cross-spectrum S_{12} and the product of the wavelet auto-spectra of the two time signals (S_{11}, S_{22}) [26]:

$$CoH(f,t) = \sqrt{\frac{|S_{12}(f,t)|^2}{S_{11}(f,t)S_{22}(f,t)}}, \sqrt{b^2 - 4ac} \qquad (21)$$

where the power spectra S_{11}, S_{22} and S_{12} are given by:

$$S_{ij}(f,t) = \int_{t-T}^{t+T} w_i^*(f,\tau) w_j(f,\tau) d\tau \qquad (22)$$

where i, j ={1, 2} and T is half time length of the Gaussian excitation pulse. Analysing the coherence in the time-frequency space, the discrepancies caused by noise appear as peaks randomly distributed while the defect reflected wave arrivals are characterised by sudden changes of the coherence along a wide frequency range (Figure 9).
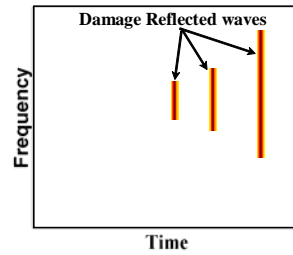

Figure 9 - Time-frequency coherence changes due to damage reflected waves.

Once the presence of damage is identified, then, the arrival times of the nonlinear damage reflected waves are evaluated. Usually, data are filtered using a pass-band filter, because of the concentration of the noise into high frequencies due to the CWT, and the poor SNR at low frequencies caused by the high frequency content of the signal discrepancy generated by the damage occurrence. Then, the arrival time of the reflected nonlinear waves [22] can be estimated by extracting the maxima lines (ridges of the arrivals of nonlinear waves reflected by damages) in the frequency time space. As result of this procedure, maxima lines may have a winding behaviour with the frequency that might affect the accuracy of the damage localisation. In this case, a least square polynomial interpolation algorithm can be used to reduce the effect of noise impact in the localisation process.
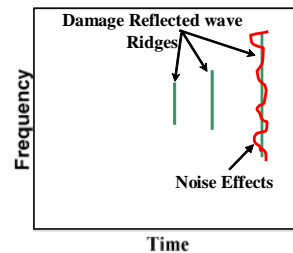

Figure 10 – Nonlinear wave arrival times.

8. Test case

The methodology above illustrated was investigated on numerically simulated data of an 8 layer composite sheet (see Table 1 and Figure 11), 400mm long and 12mm thick (1.5mm each layer), with a damage 5mm long and 4.5mm thick. Three different PM space were considered for each material variable (E_{11}, E_{22}, G_{12}).
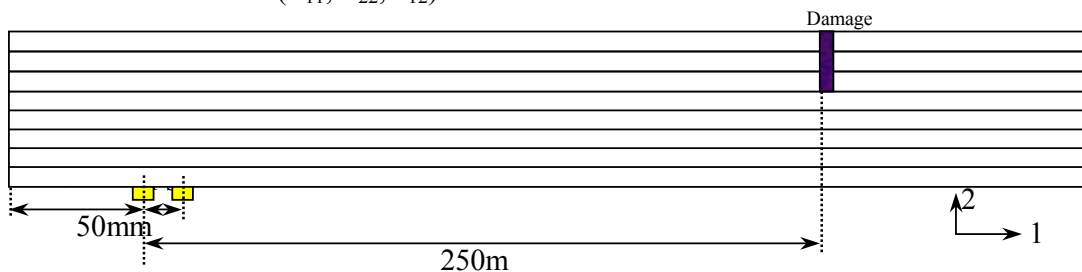

Figure 11 – Test case configuration.

	Layers (1, 3, 5, 7)	Layers (2, 4, 6, 8)
E_{11}	144.8 GPa	9.7 GPa
E_{22}	9.7 GPa	9.7 GPa
G_{12}	6 GPa	3.6 GPa
ν_{12}	0.3	0.34
ρ	$1600 kg/m^3$	$1600 kg/m^3$

Table 1 – Material characteristics.

The damage was simulated by using a uniform PM density distribution $\mu(P_c, P_o)$ (eq. 7, [31]).

$$\mu\left(P_c, P_o\right) = N\left[e^{-\left(\frac{P_c + P_o - a}{b}\right)^2 - c(P_c - P_o)} + e^{-\left(\frac{P_c + P_o + a}{b}\right)^2 - c(P_c - P_o)}\right] \qquad (23)$$

with P_c and $P_o \in [P_{min}, P_{max}]$ and $P_c \geq P_o$. Since, experimental data on hysteretic behaviour of the test case could not be found, parameterised PM space variables (Table 2, Figure 12) were estimated by experimental data available in literature for a different composite [31].

The parameters a, b, c and N (Table 2) were evaluated by using a least square optimisation algorithm to reproduce the hysteretic behaviour of a $[\pm 45]_{2s}$ laminate under tensile cyclic loading [31], κ was also considered as variable of the optimisation, since the composite failure strain is far larger than the maximum strain that was considered in the optimisation process. While P_{min} was posed equal to $-P_{max}$ and P_{max} was assumed to be the equal to the tensile failure strength of the laminate. The fitting processes resulted in a close agreement between the literature and the optimised PM space derived stress-strain curves, (Figure 13).
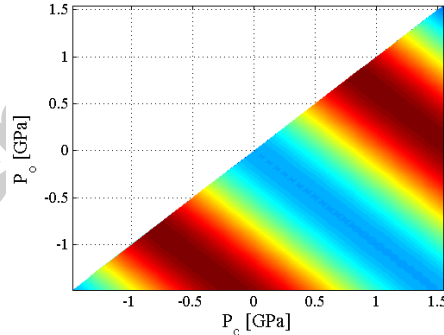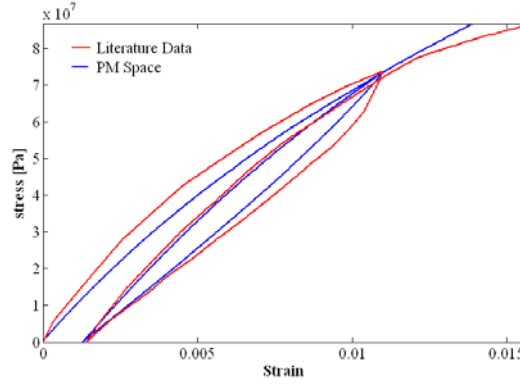

Figure 12 – Test case PM space.

Figure 13 – Comparison between optimised PM space and literature data.

Laminate	Optimised	Test Case
E (Elasticity Modulus)	9.9GPa	144.8GPa
Tensile failure strain (S_f)	0.050	0.016
Tensile failure strength (P_{max})	0.115GPa	1.545GPa
a	$1.063P_{max}$	1.643GPa
b	$0.758\ P_{max}$	1.172GPa
c	2e-12	2e-12
N	5.97e-17	3.323e-19
κ	$0.543S_f$	0.00868

Table 2 – PM space parameters.

Two piezoelectric patches (s1 and s2, 7mm long – Pz_l – and 0.2mm thick – Pz_t) were placed as showed in Figure 11. Sensor s1 was simulated in the excitation mode by applying on the test case distributed forces (F_x, F_y) as follows:

$$F_x = \frac{1}{r}(x\text{-}x_c)f(t) \quad x=[x_c\text{-}r,r+x_c]$$

$$F_y = \frac{Pz_t}{2r}\sqrt{1-\left[(x_c\text{-}x)\frac{1}{r}\right]^2}\ \Gamma(t) \qquad (24)$$

$$r = \frac{Pz_l}{2}$$

where:

- x_c is the coordinate of the sensor s1 centre.

- $$\Gamma(t) = \text{-}A\sin(2\pi ft)e^{\frac{(t\text{-}t_0)^2}{2p^2}}$$

  $f=150\text{kHz}$; $p=\frac{0.25}{f}$; $t_0=3p=T$

- f is the Gaussian pulse central frequency.
- A [N] is the signal amplitude.

Five different excitation amplitudes (5N, 20N, 40N, 80N and 160N) were investigated on the test case. These amplitudes are compatible with the strength developable by piezoelectric patches, since according to the Piezo-Kinetic Corporation database a squared piezoelectric patch (7x7mm, 0.2mm thick) made of PKI-556 is capable of developing an in-plane force of 8.81 N/V for a maximum allowable voltage of 40V. In acquisition mode, the sensors s1 and

s2 time signals s(t) were evaluated as function (eq. 9) of the stresses (σ_x, σ_y) estimated by our in-house nonlinear FE code (§4).

$$\sigma_x = \sigma_x\left(x,t\right)\big|_{y=y\_piezo}$$

$$\sigma_y = \sigma_y\left(x,t\right)\big|_{y=y\_piezo} \qquad (25)$$

$$s(t) = \left[\int_{x_c-r}^{r+x_c} \left(\sigma_x F_x\right) + \left(\sigma_y F_y\right) dx\right]$$

The element size e_L (13) of the FE model used is given by the ratio between the pulse wavelength W_L and the number of elements, NoE_{WL}, used to describe it.

$$e_L = \frac{W_L\left(f\right)}{NoE_{WL}} = \frac{0.0204m}{40} = 0.00051m \cong 0.5mm \qquad (26)$$

For wavelength W_L (14) is meant the space traveled by a pressure wave P oscillating with a frequency f (pulse central frequency) with a wave speed c_{min}. Where c_{min} (15) is the minimum P wave speed, in the structure under investigation (even layers of the composite).

$$W_L\left(f\right) = \frac{c_{min}}{f} = \frac{3055\frac{m}{s}}{150kHz} = 0.0204m \qquad (27)$$

$$c_{min} = \sqrt{\frac{E(1-v)}{\rho(1+v)(1-2v)}} = \sqrt{\frac{9.7GPa(1-0.34)}{1600kgm^{-3}(1+0.34)(1-0.68)}} = 3055\frac{m}{s} \qquad (28)$$

Finally, the time integration step dt, used was estimated as the time employed by the quickest P wave (c_{max}, odd layers of the composite, eq. 17) to cross a finite element (e_L), times a safe factor S_F:

$$dt = S_F \frac{e_L}{c_{max}} = 0.25\frac{0.0005m}{11038\frac{m}{s}} = 1.2x10^{-8}s \qquad (29)$$

$$c_{max} = \sqrt{\frac{E(1-v)}{\rho(1+v)(1-2v)}} = \sqrt{\frac{144.8GPa(1-0.3)}{1600kgm^{-3}(1+0.3)(1-0.6)}} = 11038\frac{m}{s} \qquad (30)$$

9. Results

In this section, the capability of the TNEWS to detect damage is shown. A detailed analysis of the effects of the change of excitation amplitude and sampling frequency on the TNEWS accuracy is also presented.

9.1. TNEWS procedure results

The CTW of the simulated time signals acquired at the two sensor locations (s1, s2) for two different excitation amplitudes (A_1=5N and A_2=40N) was estimated. A complex Morlet wavelet with a central frequency $f_0 = 7$ and a wavelet frequency band $\gamma = 0.25$ was used. An example on the CWT performed on sensors s1 and s2 due to the excitation amplitude A_1 is given in Figure 14.
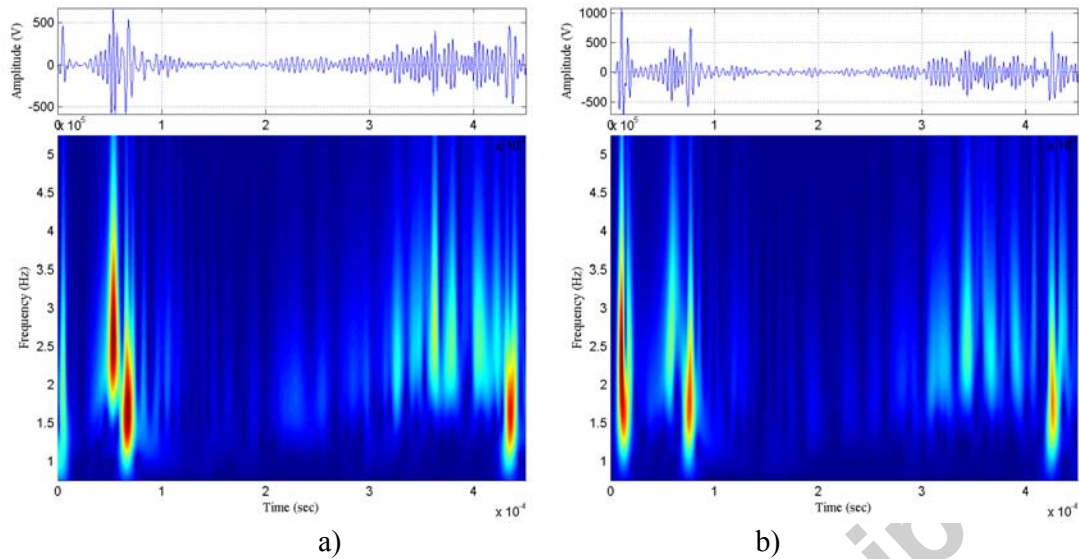
Figure 14 – CWT of time signal: a) sensor s1; b) sensor s2.

By analysing the time-frequency coherence, the presence of damage was identified, since the time-frequency ridges due to the arrivals of the damage reflected perturbation waves can be clearly observed ((a)   (b)

Figure 15). As expected the drop of coherence (ridges) are associated with a frequency content shaped around the third harmonic of the pulse central excitation frequency, in line with the non classical non linearity prediction described in paragraph 3.
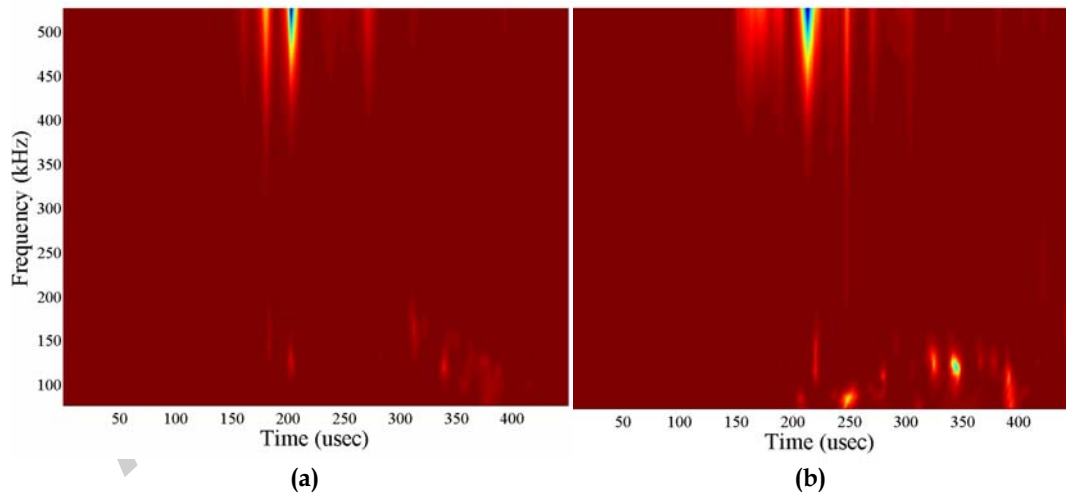

(a)   **(b)**

Figure 15 – Time-Frequency Coherence: a) sensor s1; b) sensor s2.

Once, the damage presence was detected, the arrival time curves were extracted by an automatic algorithm that selects the first reflected wave maxima lines for each sensor (Figure 16). Finally, the damage localisation can be carried out using the maxima lines labelled with 1 in Figure 16-a and b and eq. 17. As result of this process, the damage (see blue line in

Figure 17) is plotted as a function of the frequency and it can be seen that it was localised with the change of the frequency within the tolerance of the methodology due to the piezoelectric patch finite dimension (±3.5mm, see the red line in

Figure 17) and to the wavelength of the impinging/damage reflected perturbation (see the green line in
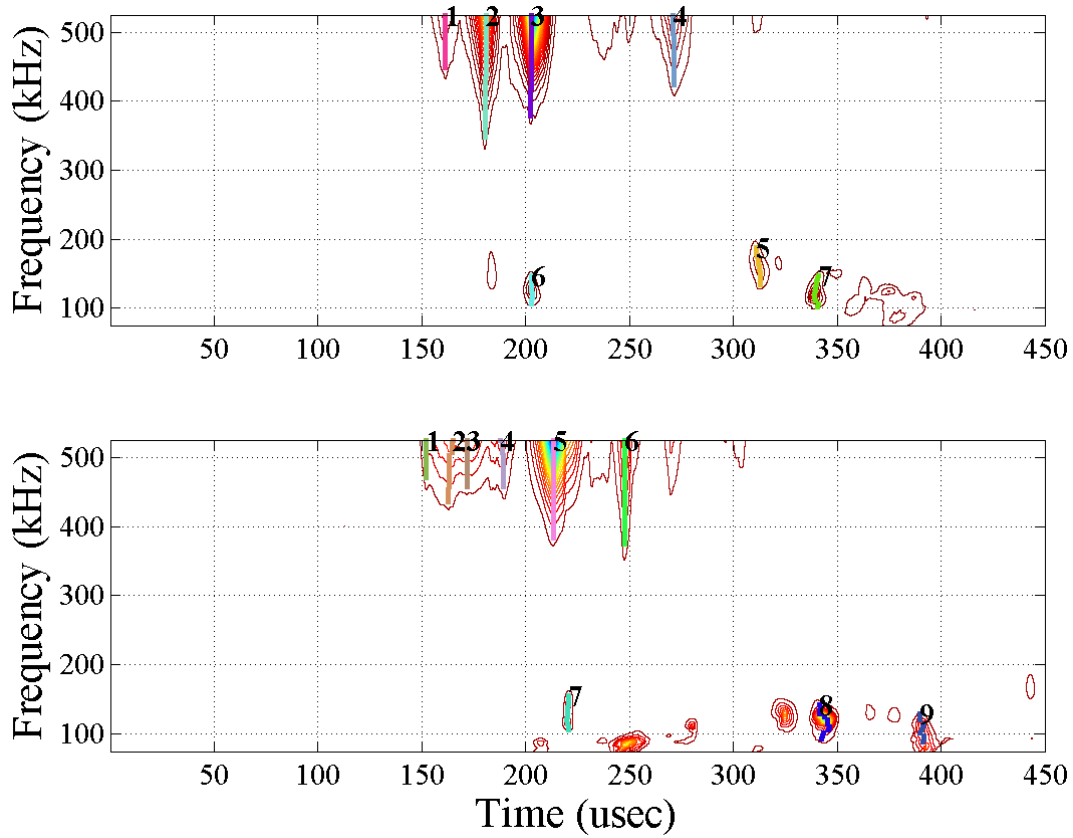
Figure 17).

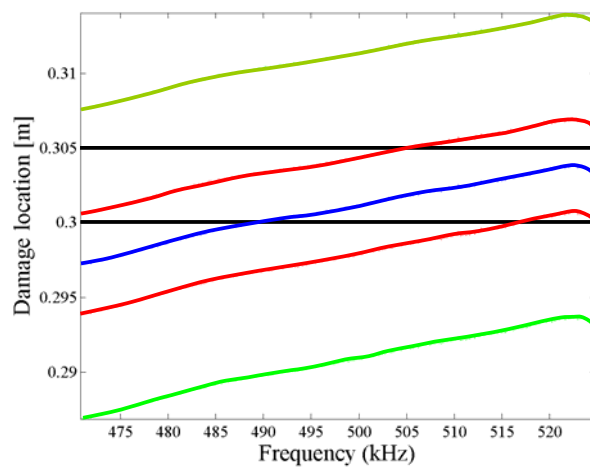**Figure 16 – Maxima lines extraction: a) sensor s1; b) sensor s2.**

Figure 17 – Damage predicted location from left edge of the composite plate section.

9.2. Effects of excitation amplitude changes on the TNEWS accuracy

According to theory and experimental evidences ([2-10, 11-14], §2-3,7), the non-classical nonlinear elastic material behaviour increases with the excitation pulse amplitude and, consequently, the TNEWS detected uncorrelation amplitudes between the nonlinear components of damage reflected waves should increase with the difference of the excitation pulse amplitudes $\Delta A = A_2 - A_1$. In order to investigate this phenomenon, the excitation amplitude A_1 was kept constant to 5N, while A_2 was changed between {20N, 40N, 80N, 160N}, as sampling time was used the time integration step dt evaluated by eq. 16 (sampling frequency 83.3MHz). Differently from the predictions made before, the results displayed in Figure 18 (the predicted localisation curves are named according to $A_1\_A_2N$) showed that for A_2 ranging between 20N and 80N, no significant change in terms of improved accuracy of the damage localisation. On the other hand, the frequency range in which is possible locating the damage seemed increasing with A_2. Furthermore, for $A_2=160N$, a large improvement of damage localisation accuracy was obtained (see curve 5_160N in Figure 18). These remarks highlighted that is not only ΔA but also the level of A_2 plays a fundamental role on the accuracy of the TNEWS.
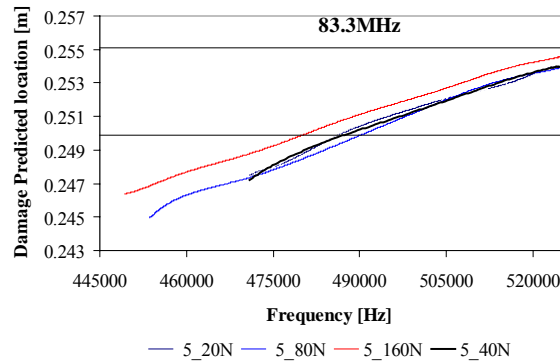

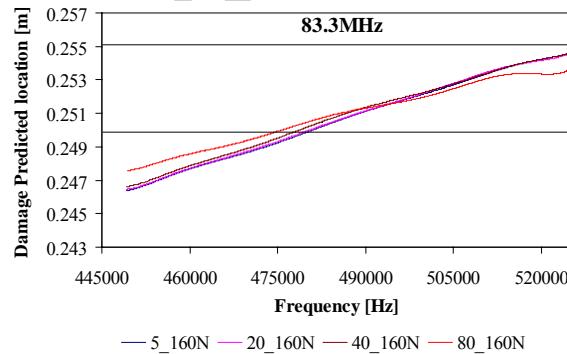**Figure 18 – Damage predicted locations (referred to s_1): $A_1=5N$ and $A_2=$ {20N, 40N, 80N, 160N}.**

Figure 19 – Damage predicted locations (referred to s_1): $A_1=$ {5N, 20N, 40N, 80N} and $A_2=160N$.

In order to understand the effect of A_2 on the TNEWS accuracy, the damage detection process was performed keeping constant A_2 at 160N and changing $A_1=$ {5N, 20N, 40N, 80N}. The outcomes of such investigation showed (Figure 19) that the increase of A_1 had no apparent change on the detection frequency range. Moreover, as in the case of A_2, changing A_1 from 5 to 40 had small effects on the TNEWS accuracy, however, a consistent enhancement of the TNEWS accuracy was obtained with $A_1=80N$. This last evidence casts shadows on the importance of ΔA and highlights the need of further insights on non-classical nonlinear elastic mechanisms, since the best accuracy is given by a set of excitation amplitudes (80_160N) having a ΔA of 80N against the 155N of the 5_160N curve, which also appeared to be the worst. Therefore, a key role in the TNEWS process is played not only by

A_2 and in some extent by ΔA but also by A_1.   Furthermore, using excitation amplitude A_1 larger than 80N seems to constitute a sort of threshold above which the damage localisation accuracy increases, these evidences are in the limit of the PM space model used and further attempt of analysing the results can be considered mere speculations, therefore, an extensive experimental campaign will be needed to validate these results.

9.3. Effects the sampling frequency on the TNEWS accuracy

The effect of sampling frequency on the accuracy and run-time of the developed damage detection process was investigated. In particular, the time signals with the following sampling frequency 41.7 MHz, 20.8 MHz, 10.4 MHz and 5.2 MHz were analysed. The time length of the detection process varies from 20min for 41.7 MHz to 1min 20 sec for 5.2MHz. However, the TNEWS accuracy (Figure 20) was affected just marginally as the error of the predicted damage location was comparable with that of the least accurate A_1 and A_2 combinations (see 5_20N in Figure 18). Moreover, an increasing wobbling of the damage localisation lines can be observed with the sampling frequency reduction (Figure 20-Figure 21), though, the errors are well within into the tolerance limits showed in
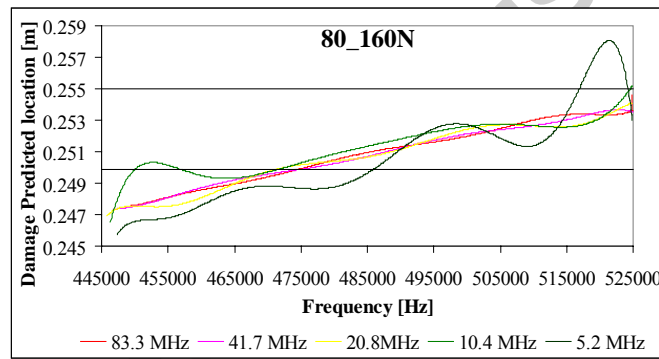
Figure 17, i.e. about ±10mm.

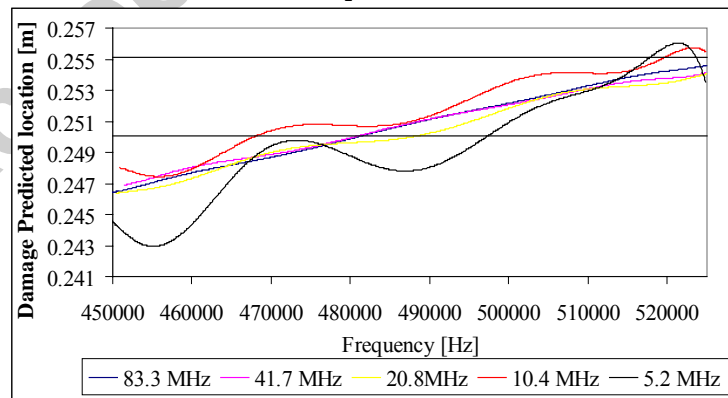**Figure 20 – Effect of the sampling frequency on damage predicted locations (referred to s₁): A₁=80N and A₂=160N.**

Figure 21 – Effect of the sampling frequency on damage predicted locations (referred to s₁): A₁=5N and A₂=160N.

Conclusions

In this paper, a new transient nonlinear elastic wave spectroscopy is presented for the detection and localization of damage in composite plate. The damaged area was modelled using a multi-scale material constitutive model (Preisach-Mayergoyz space). The damage detection methodology is articulated in three steps. In the first step, the presence of the damage on the structure is assessed. In the second step, the arrival time of the reflected wave (or echo) can be estimated, and in the third step the damage location through a simplified Ray-Tracing algorithm is detected.

The developed technique identified in a clear manner the faulted zone showing its robustness to detect and locate nonlinear sources in presence of multilayer material.

References

1. C. Santulli, "Impact damage Evaluation in woven composites using acoustic and thermoelastic techniques, Ph. D. Dissertation, Liverpool University, 2000

2. K. Van Den Abeele, P. A. Johnston, A. Sutin, Nonlinear elastic wave spectroscopy (NEWS) techniques to discern material damage, part I: nonlinear wave modulation spectroscopy (NWMS), Res. Nondestr Eval, Vol. 12(1), pp. 17-30, 2000.

3. R. A. Guyer, P. A. Johnson, Nonlinear mesoscopic elasticity: evidence for a new class of materials, Physics Today, pp 30-36, April 1999.

4. P. Johnston, The new wave in acoustic testing, Materials World, Vol. 7(9), pp. 544-46, 1999.

5. K. Van Den Abeele, J. De Visscher, Damage assessment in reinforced concrete using spectral and temporal nonlinear vibration techniques, Cement and Concrete Research, Vol: 30(9), pp. 1453-1464, 2000.

6. C. Campos-Pozuelo, J. A. Gallego-Juárez, Experimental Analysis Of The Nonlinear Behaviour Of Fatigued Metallic Samples, WCU 2003, Paris, September 7-10, 2003.

7. K. Van Den Abeele, J. Carmeliet and M. Wevers, Quantification of microdamage in slate tiles: comparison of nonlinear acoustic resonance experiments with visual and X-ray diagnosis, ISNA, Gottingen, 1999.

8. K. E-A. Van Den Abeele, A.Sutin, J.Carmeliet and P.A. Johnson, Micro-damage diagnostics using Nonlinear Elastic Wave Spectroscopy (NEWS), NDT&E International, Vol. 34, pp. 239-248, 2001.

9. K. Van Den Abeele, K. Van de Velde, J. Carmeliet, Inferring the degradation of pultruded composites from dynamic nonlinear resonance measurements, Polymer Composites, Vol. 22(4), pp. 555-567, 2001.

10. M. Meo, G. Zumpano, Impact Damage identification on sandwich plates through Nonlinear Elastic Wave Spectroscopy, ICCST/5 - 5th International conference on Composite Science and Technology, Sharjah – UAE, 1-3 2005.

11. K. Van Den Abeele, P. A. Johnston, A. Sutin, Nonlinear elastic wave spectroscopy (NEWS) techniques to discern material damage, part II: Single Mode Nonlinear Resonance Acoustic Spectroscopy, Research on NonDestructive Evaluation 12, 31-43, 2000.

12. M. Meo, G. Zumpano, U. Polimeno, Corrosion identification on an aluminium plate-like structure by monitoring wave propagation phenomena, First World Congress on Corrosion in the Military, Sorrento, Italy, 6-8 June 2005.

13. G. Zumpano, M. Meo, Finite Element Simulation of Wave Propagation Phenomena in a Damaged Plate to Support Development of Nonlinear Elastic Wave Spectroscopy Techniques, NDT in Progress, Prague, October,10-12, 2005.

14. M. Meo, G. Zumpano, Stress Corrosion Cracking Identification and Localisation through Nonlinear Elastic Wave Self Focusing using Time Reversal Mirrors in Welded Plate-Like Structures, submitted to International Journal of Solids and Structures, December 2005.

15. L. D. Landau, E. M. Lifshitz, Theory of Elasticity, Pergamon, Tarrytown, NY 1959.

16. K. R. McCall, R. A. Guyer, Equation of state and wave propagation in hysteretic nonlinear elastic materials, Journal of Geophysical Research, Vol. 99(B12), pp. 23887-23897, 1994.

17. K. R. McCall, R. A. Guyer, A new theoretical paradigm to describe hysteresis, discrete memory and nonlinear elastic wave propagation in rock, Nonlinear Processes in Geophysics, Vol. 3, pp. 89-101, 1996.

18. Y. M. Hu, W. Floer, U. Krupp and H. -J. Christ, Microstructurally short fatigue crack initiation and growth in Ti-6.8Mo-4.5Fe-1.5Al, Materials Science and Engineering A, Vol. 278(1-2), pp. 170-180, 1999.

19. P. Konhke, ANSYS Inc. Theory manual – Twelfth Edition, SAS IP Inc., 2001.

20. K.-J. Bathe, Finite element procedures in engineering analysis, Prentice-Hall Inc., 1982.

21. R. D. Cook, D. S. Malkus, M. E. Plesha, Concepts and applications of finite element analysis – 3rd Edition, John Wiley & Sons, 1989.

22. G. Zumpano, M. Meo, A new damage detection technique based on wave propagation for rails, International Journal of Solids and Structures, Vol. 43(5), pp. 1023-1046, 2006.

23. L. Angrisani, P. Daponte, Thin thickness measurements by means of a wavelets transform-based method, Measurement, Vol. 20(4), pp. 227-242, 1997.

24. V. C. Chen, H. Ling, Time-Frequency Transformation for Radar Imaging and Signal Analysis, Artech House, Boston, London, 2002.

25. S. Mallat, A wavelet tour of signal processing, London: Academic Press, 1998.

26. Teolis, Computational signal processing with wavelets, Birkhauser: Boston, 1998.

27. Kareem, T. Kijewski, Time-frequency analysis of wind effects on structures, Journal of Wind Engineering and Industrial Aerodynamics, Vol. 90, pp. 1435-1452, 2002.

28. S. Legendre, J. Goyette, D. Massicotte, Ultrasonic NDE of composite material structures using wavelets coefficients, NDT&E International, Vol. 34(1), pp. 31-37, 2001.

29. X. Gilliam, J. Dunyak, A. Doggett, D. Smith, Coherent structure detection using wavelet analysis in long time-series, J. of Wind Engineering and Industrial Aerodynamics, Vol. 88, pp. 183-195, 2000.

30. W. J. Staszwski, Identification of damping in MDOF systems using time-scale decomposition, J. of Sound and Vibration, Vol. 203(2), pp. 283-305, 1997.
31. K. Van Den Abeele, F. Schubert, V. Aleshin, F. Windels, J. Carmeliet, Resonant bar simulations in media with localised damage, Ultrasonics, Vol. 42, pp. 1017-1024, 2004.
32. L. Greve, A. K. Pickett, Delamination testing and modelling for composite crash simulation, Composites Science and Technology (2006) Vol. 66 pp. 816 -826.